

QUANTUM PHYSICS

Quantum gate teleportation between separated qubits in a trapped-ion processor

Yong Wan^{1,2,*†}, Daniel Kienzler^{1,2,†‡}, Stephen D. Erickson^{1,2}, Karl H. Mayer^{1,2}, Ting Rei Tan^{1,2,§¶}, Jenny J. Wu^{1,2}, Hilma M. Vasconcelos^{1,2,3}, Scott Glancy¹, Emanuel Knill¹, David J. Wineland^{1,2,4}, Andrew C. Wilson¹, Dietrich Leibfried¹

Large-scale quantum computers will require quantum gate operations between widely separated qubits. A method for implementing such operations, known as quantum gate teleportation (QGT), requires only local operations, classical communication, and shared entanglement. We demonstrate QGT in a scalable architecture by deterministically teleporting a controlled-NOT (CNOT) gate between two qubits in spatially separated locations in an ion trap. The entanglement fidelity of our teleported CNOT is in the interval (0.845, 0.872) at the 95% confidence level. The implementation combines ion shuttling with individually addressed single-qubit rotations and detections, same- and mixed-species two-qubit gates, and real-time conditional operations, thereby demonstrating essential tools for scaling trapped-ion quantum computers combined in a single device.

Quantum computers have the potential to solve problems that are intractable for conventional computers. However, many quantum bits (qubits) are required to outperform conventional computing capabilities, and scaling quantum computers to be useful in practical applications is difficult (1). As the system size increases, the average distance between qubits grows, making it harder to connect arbitrary qubits. Quantum gate teleportation (QGT) is a uniquely quantum solution that enables logical gates between spatially separated qubits, where shared entanglement eliminates the need for a direct quantum coherent interaction (2, 3).

There are several proposals for scaling up to larger numbers of qubits in trapped-ion systems. These include the quantum charge-coupled device (QCCD) architecture, which incorporates a large array of segmented electrodes to create trapping zones specialized for roles such as loading ions, processing, and memory storage (4, 5). Qubits can interact by being physically moved to the same zone. A variant of this approach couples different zones by creating entanglement via a photonic network (6). Both approaches will benefit from a way to perform gate operations between separated qubits via QGT, which mitigates latency from transmitting quantum information between zones, provided

that the required entangled ancilla pairs are prepared and distributed ahead of time during unrelated processor functions. This entanglement can be produced using various methods, including unitary gates, dissipative schemes (7), and photonic links (8).

Progress toward distributed quantum computation has been made with quantum state teleportation (9), where an arbitrary state is transferred between remote parties (2, 10). Using state teleportation, a two-qubit gate between two parties, Alice and Bob, can be implemented by teleporting Alice's input state to Bob, applying local two-qubit gates at Bob's location, and teleporting Alice's half of the output back to her. This process consumes a minimum of two shared entangled pairs.

For a controlled-NOT (CNOT) gate, the task can be achieved more efficiently using the protocol depicted in Fig. 1A (3) without the need to physically bring the qubits together or teleport the states back and forth. This protocol achieves the minimum possible overhead, requiring only local operations, classical communication, and a single entangled pair shared between two locations. The protocol implementing a teleported CNOT between qubits B_1 and B_2 works as follows. The initial entanglement between qubits M_1 and M_2 is transferred to B_1 and M_2 through the first local CNOT, M_1 detection, and conditional operation on M_2 . With the information about B_1 's state now shared with M_2 , B_1 is the effective control of the second local CNOT that acts on B_2 . The remaining operations serve to disentangle M_2 from B_1 and B_2 , resulting in an effective CNOT between B_1 and B_2 . This type of teleported gate has been demonstrated probabilistically with photonic systems, where the required conditional operations were implemented with passive optical elements and post-selection (11, 12). More recently, a deterministic

CNOT was teleported between two superconducting cavity qubits using an entangled pair of transmons (13).

Here, we demonstrate a deterministic teleported CNOT between two ${}^9\text{Be}^+$ ions using a shared entangled pair of ${}^{25}\text{Mg}^+$ ions. This demonstration combines key elements for scalable quantum computation with trapped ions, including separation and transport of mixed-species ion crystals, local same- and mixed-species two-qubit gates (14), individually addressed single-qubit rotations and detection, and conditional operations based on measurement results. We use quantum process tomography (QPT) to characterize the teleported CNOT. We simplify the demonstration by using only one laser interaction zone (LIZ) and transporting the separated qubits to this location, but the key elements of the protocol are retained.

Our experiment uses two ${}^9\text{Be}^+$ ions (B_1, B_2) and two ${}^{25}\text{Mg}^+$ ions (M_1, M_2) trapped in a segmented linear Paul trap. The qubits are encoded in the $|F = 1, m_F = 1\rangle_B \equiv |\uparrow\rangle_B$ and $|2, 0\rangle_B \equiv |\downarrow\rangle_B$ hyperfine states of ${}^9\text{Be}^+$ and the $|2, 0\rangle_M \equiv |\uparrow\rangle_M$ and $|3, 1\rangle_M \equiv |\downarrow\rangle_M$ states of ${}^{25}\text{Mg}^+$. We use the symbol B (M) for ${}^9\text{Be}^+$ (${}^{25}\text{Mg}^+$) ions and label respective states with subscript B (M). To begin each experiment, a four-ion chain is initialized in the order $B_1-M_1-M_2-B_2$ in a potential well where all laser beams pass through the trap, a region we refer to as the LIZ (Fig. 2). Qubit-state measurements of B (M) ions are realized by state-dependent fluorescence detection with 313 nm (280 nm) resonant light after transferring the population from the computational basis to the measurement basis $|\uparrow\rangle_B \rightarrow |2, 2\rangle_B \equiv |\text{Bright}\rangle_B$ and $|\downarrow\rangle_B \rightarrow |1, -1\rangle_B \equiv |\text{Dark}\rangle_B$ ($|\downarrow\rangle_M \rightarrow |3, 3\rangle_M \equiv |\text{Bright}\rangle_M$ and $|\uparrow\rangle_M \rightarrow |2, -2\rangle_M \equiv |\text{Dark}\rangle_M$) (15). Segmented trap electrodes enable the use of time-varying potentials to split the ion crystal into selected subsets and to transport them to and from the LIZ (16, 17). Spatial separation enables individual addressing of ions of the same species, whereas ions of different species are distinguished by their well-separated resonant wavelengths.

Stimulated Raman transitions are used for all coherent qubit operations. A pair of copropagating laser beams for each species drives single-qubit rotations $\hat{R}(\theta, \phi)$, and rotation around the z -axis $\hat{R}_Z(\alpha)$ is implemented by phase-shifting all subsequent single-qubit rotations for that qubit (15). A pair of perpendicular laser beams for each species drives two-qubit Mølmer-Sørensen (MS) entangling gates (18). Both pairs of Raman beams are applied simultaneously to drive mixed-species MS gates (14). We construct $\text{CNOT}_{C \rightarrow T}$ (C for control and T for target) and the Bell-state-generating gate \hat{F} using single-qubit rotations and MS gates (14, 15, 19).

The circuit diagram for our teleported CNOT is shown in Fig. 1B, and ion configurations during QGT are illustrated in Fig. 2. After ground-state cooling of the four-ion chain, the algorithm begins with the B and M ions in $|\text{Bright}\rangle_B$ and $|\downarrow\rangle_M$, respectively. \hat{F} is applied to the two M ions to generate the Bell state $|\Phi^+\rangle_M = \frac{1}{\sqrt{2}}(|\uparrow\rangle_M + |\downarrow\rangle_M)$ (Fig. 2A). Afterwards, the chain is split

¹National Institute of Standards and Technology, Boulder, CO 80305, USA. ²Department of Physics, University of Colorado, Boulder, CO 80309, USA. ³Departamento de Engenharia de Teleinformática, Universidade Federal do Ceará, Fortaleza, Ceará, 60440, Brazil. ⁴Department of Physics, University of Oregon, Eugene, OR 97403, USA.

*Corresponding author. Email: yong.wan@nist.gov

†These authors contributed equally to this work. ‡Present address: Institute for Quantum Electronics, ETH Zürich, 8093 Zürich, Switzerland. §Present address: Department of Physics, National University of Singapore, 117551 Singapore. ¶Present address: Centre for Quantum Technologies, 117543 Singapore.

into two B-and-M pairs in separated regions of a double-well potential (Fig. 2B), which is translated to bring B_1 - M_1 into the LIZ. There, we ground-state cool B_1 - M_1 by addressing B_1 , prepare B_1 to its input state, and apply $CNOT_{B_1 \rightarrow M_1}$. Then, M_1 is detected (Fig. 2C). Its qubit state is determined by comparing the number of detected photons to a preset threshold. The double-well potential is then translated to move M_2 - B_2 into the LIZ, where the pair is ground-state cooled by addressing B_2 . Qubit B_2 is then prepared in its input state, and the conditional operation $\hat{R}(\pi, 0)$ is applied on M_2 if M_1 was measured to be in $|\downarrow\rangle_M$. Next we apply $CNOT_{M_2 \rightarrow B_2}$, followed by a rotation $\hat{R}(\frac{\pi}{2}, -\frac{\pi}{2})$ and detection of M_2 . A rotation selecting the measurement axis for state tomography is applied to B_2 , which is then mapped out to the measurement basis, but not yet detected (Fig. 2D). This mapping reduces the depumping of B_2 from stray scattered light when detecting B_1 later in the process. The double-well potential is translated back to bring B_1 - M_1 into the LIZ, where we apply the conditional operation $\hat{R}_Z(\pi)$ if M_2 was measured to be in $|\downarrow\rangle_M$, followed by a single-qubit rotation selecting the measurement axis and a measurement of B_1 (Fig. 2E). Subsequently, M_2 - B_2 are shuttled back into the LIZ where B_2 is detected (Fig. 2F). At the end of this sequence, the four ions are recombined into a single well to prepare for the next repetition of the experiment.

We used QPT (20) to characterize our teleported CNOT between the two B ions. We implemented 144 different combinations of input states and measurement axes in random order, each for ~300 consecutive experiment executions. Two complete sets of tomography data (dataset 1 and dataset 2) were acquired. We developed a protocol for data analysis on dataset 1 while remaining blind to dataset 2 and then applied this protocol to dataset 2. The analysis methods and results for dataset 2 are summarized below.

From the observed measurement outcomes, we determined the most likely quantum process by maximum likelihood (ML) estimation and inferred a 95% confidence interval of (0.845, 0.872) for the entanglement fidelity with respect to an ideal CNOT. The matrix representing the quantum process is shown in Fig. 3. For details of our analysis, see (15).

Ideally, the observed data should be consistent with the assumption of a single quantum process, but drifts in control parameters on time scales much longer than that of a single QGT experiment can lead to imperfections. To detect departure from this assumption, we applied a likelihood ratio (LR) test (21, 22). An LR was computed from the experimental data and compared to the distribution of LRs obtained from synthetic datasets generated by parametric bootstrapping (23). The test indicated that our data was inconsistent with a single quantum process (15). Motivated by this finding, we discovered drifts in single-qubit-rotation angles that eluded our feedback mechanisms but that can be addressed in future experiments (15). Using

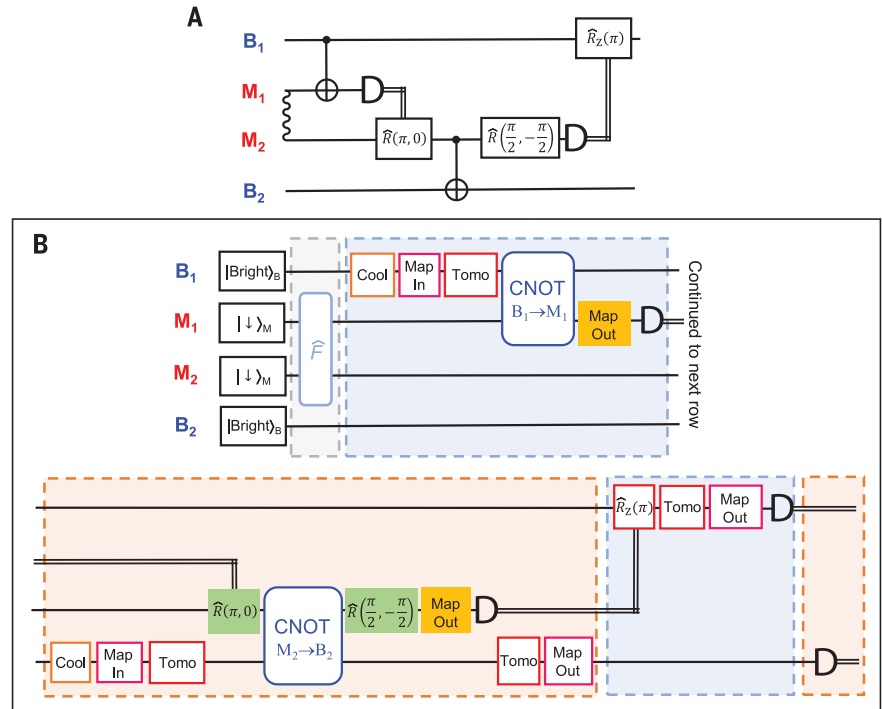


Fig. 1. QGT circuit diagram. (A) Circuit diagram for a teleported CNOT between qubits B_1 and B_2 as proposed in (3). The wavy line represents entanglement, and double solid lines represent classical communication. (B) Experiment-specific circuit diagram for the teleported CNOT gate between B_1 and B_2 . “Map In” indicates mapping from the measurement basis to the computational basis, and “Map Out” indicates the opposite process. “Tomo” refers to single-qubit rotations for QPT.

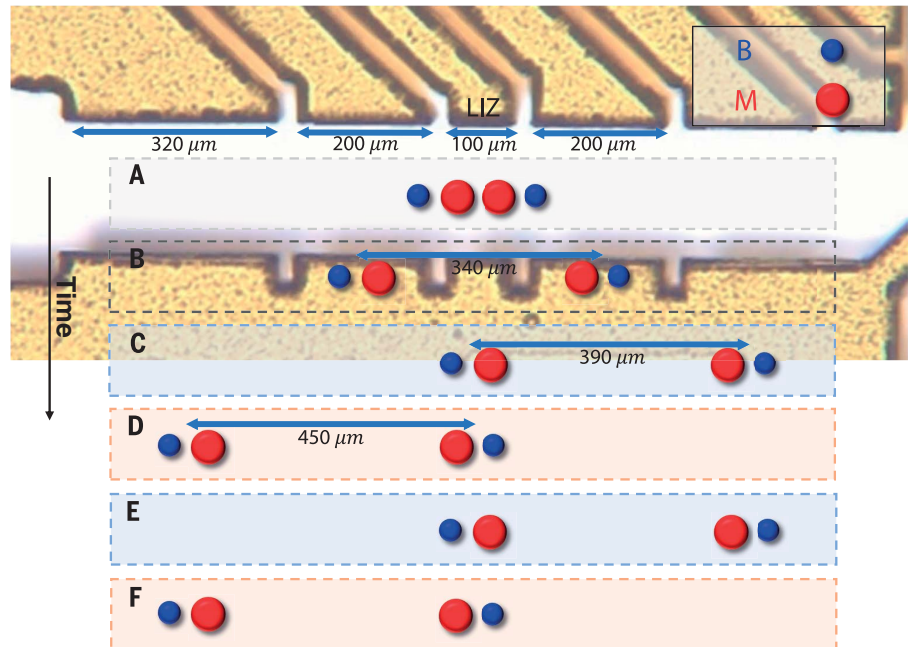


Fig. 2. QGT shuttling sequence. (A to F) The shuttling sequence, overlaid on a photograph of a section of the trap electrode structure (ions and ion spacings are not to scale). After preparing the M ions in a Bell state to serve as the entanglement resource, the B_1 - M_1 - M_2 - B_2 chain is split into two B-and-M ion pairs, which are translated into and out of LIZ to address and detect individual ions (C to F).

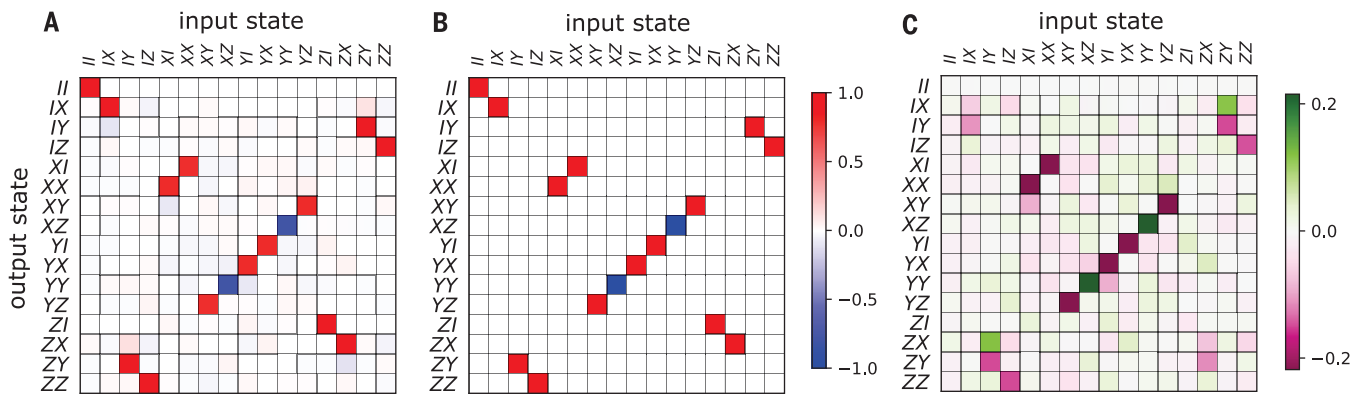


Fig. 3. Pauli transfer matrix. Visualization of quantum processes in the Pauli transfer matrix representation for (A) the experimental dataset 2, (B) the ideal CNOT process, and (C) the difference between the experimental and ideal process matrices (15). The Pauli transfer matrix of a process maps an arbitrary

input density matrix, expressed as a linear combination of Pauli products, into the corresponding linear combination that describes the output density matrix. For our implementation, a 95% confidence interval (0.845, 0.872) for the entanglement fidelity is determined with respect to an ideal CNOT.

Table 1. Error sources for the teleported CNOT. The Bell-state fidelity with state preparation and measurement (SPAM) error contributions subtracted is used as an estimate of the mixed-species CNOT fidelity (15). 1σ uncertainty for the respective error sources is shown in parentheses.

Source	Error (10^{-2})
SPAM on two B ions	1.1(7)
SPAM on two M ions	1.5(3)
M_1 - M_2 Bell state	4.0(9)
B_1 - M_1 CNOT	3.0(9)
M_2 - B_2 CNOT	3(1)
Coherence of M ions	0.7(3)
Stray light from	1.1(4)
M_1 detection on M_2	
Stray light from	1.2(3)
B_2 cooling on B_1	
Sum	16(2)
Depolarizing model	12(1)

numerical simulation, we verified that realistic fluctuations of single-qubit-rotation angles are capable of causing an inconsistency comparable to that observed in our data. Although such drifts are not major sources of infidelity for this experiment (15), such consistency checks could be an important diagnostic that can supplement other benchmarking techniques and uncover overlooked sources of infidelity.

We list the dominant error sources and estimate their combined impact in Table 1. If all errors are mutually independent, the total error is 0.16(2). A depolarizing model provides a more accurate description of the impact of individual errors and predicts a process fidelity of 0.88(1), which is near the upper limit of the 95% ML confidence interval, indicating that the major

error sources are included in the error propagation model (15).

Ideally, QGT would be implemented using an ion species with a transition insensitive to magnetic field fluctuations, to serve as both information-carrying qubits and entanglement-resource qubits, and a second dedicated species for cooling. This would mitigate decoherence and allow QGT to be embedded in a larger quantum circuit (in our experiment, any prior information encoded in B_1 and B_2 would be destroyed during cooling). Errors from stray light scattering could also be removed by using the coolant species for quantum logic readout (24). To be viable for fault-tolerant error correction, larger algorithms like QGT will also require constituent operations to be performed with higher fidelity in multiple locations. A larger QCCD array would then have many different interaction zones and integrated detection zones (25). The fact that our experimental duty cycle was dominated by shuttling and associated recoiling (15) emphasizes the importance of cold diabatic transport (26, 27) and faster cooling techniques (28).

Deterministic teleported CNOT gates can serve as a useful primitive for large-scale quantum computation. The integration of several operations, including mixed-species coherent control, ion transport, and entangling operations on selected subsets of qubits, will be essential for building large-scale quantum computers based on ions in the QCCD architecture. Moreover, applying consistency checks to the experimental data facilitated the identification of error sources in the experimental setup, illustrating the importance of performing such checks in addition to tomography when characterizing quantum processes. Similar consistency checks could be done between disjunct processing nodes executing the same routine, exposing compromised nodes that behave differently from the rest.

REFERENCES AND NOTES

- J. Preskill, *Quantum* **2**, 79 (2018).
- D. Gottesman, I. L. Chuang, *Nature* **402**, 390–393 (1999).

- J. Eisert, K. Jacobs, P. Papadopoulos, M. B. Plenio, *Phys. Rev. A* **62**, 052317 (2000).
- D. J. Wineland et al., *J. Res. Natl. Inst. Stand. Technol.* **103**, 259–328 (1998).
- D. Kielpinski, C. Monroe, D. J. Wineland, *Nature* **417**, 709–711 (2002).
- C. Monroe et al., *Phys. Rev. A* **89**, 022317 (2014).
- Y. Lin et al., *Nature* **504**, 415–418 (2013).
- D. L. Moehring et al., *Nature* **449**, 68–71 (2007).
- S. Pirandola, J. Eisert, C. Weedbrook, A. Furusawa, S. L. Braunstein, *Nat. Photonics* **9**, 641–652 (2015).
- C. H. Bennett et al., *Phys. Rev. Lett.* **70**, 1895–1899 (1993).
- Y.-F. Huang, X.-F. Ren, Y.-S. Zhang, L.-M. Duan, G.-C. Guo, *Phys. Rev. Lett.* **93**, 240501 (2004).
- W.-B. Gao et al., *Proc. Natl. Acad. Sci. U.S.A.* **107**, 20869–20874 (2010).
- K. S. Chou et al., *Nature* **561**, 368–373 (2018).
- T. R. Tan et al., *Nature* **528**, 380–383 (2015).
- Materials and methods are available as supplementary materials.
- R. B. Blakestad et al., *Phys. Rev. Lett.* **102**, 153002 (2009).
- R. B. Blakestad et al., *Phys. Rev. A* **84**, 032314 (2011).
- A. Sørensen, K. Mølmer, *Phys. Rev. Lett.* **82**, 1971–1974 (1999).
- P. J. Lee et al., *J. Opt. B Quantum Semiclassical Opt.* **7**, S371–S383 (2005).
- I. L. Chuang, M. A. Nielsen, *J. Mod. Opt.* **44**, 2455–2467 (1997).
- G. Casella, R. L. Berger, *Statistical Inference* (Cengage Learning, 2001), p. 374.
- R. Blume-Kohout et al., *Nat. Commun.* **8**, 14485 (2017).
- B. Efron, R. J. Tibshirani, *An Introduction to the Bootstrap* (CRC Press, 1994).
- P. O. Schmidt et al., *Science* **309**, 749–752 (2005).
- D. H. Slichter et al., *Opt. Express* **25**, 8705–8720 (2017).
- R. Bowler et al., *Phys. Rev. Lett.* **109**, 080502 (2012).
- A. Walther et al., *Phys. Rev. Lett.* **109**, 080501 (2012).
- C. F. Roos et al., *Phys. Rev. Lett.* **85**, 5547–5550 (2000).
- Y. Wan, Data for “Quantum gate teleportation between separated qubits in a trapped-ion processor,” Version 1, National Institute of Standards and Technology (2019); <https://doi.org/10.18434/M32056>.

ACKNOWLEDGMENTS

We thank P. Hou and D. Cole of the NIST Ion Storage Group for helpful comments on the manuscript. We thank D. T. C. Allcock and S. C. Burd (both of the NIST Ion Storage Group) and the Oxford University and the ETH Zürich ion trapping groups for their advice on stabilizing magnetic fields. **Funding:** This work was supported by the Office of the Director of National Intelligence (ODNI) Intelligence Advanced Research Projects Activity (IARPA), ONR, and the NIST Quantum Information Program. D.K. acknowledges support from the Swiss National Science

Foundation under grant 165208. S.D.E. acknowledges support by the U.S. National Science Foundation under grant DGE 1650115. Y.W., D.K., J.J.W., and H.M.V. are associates in the Professional Research Experience Program (PREP) operated jointly by NIST and University of Colorado Boulder. H.M.V. acknowledges support from the Schlumberger Foundation's Faculty for the Future program.

Author contributions: Y.W. and D.K. performed the majority of experiments with assistance from S.D.E., T.R.T., and J.J.W. D.J.W., A.C.W., and D.L. advised on the project. K.H.M.,

H.M.V., S.G., and E.K. developed statistical models and provided support on all theoretical aspects of this work. Y.W., D.K., and K.H.M. contributed to data analysis. Y.W., S.D.E., and K.H.M. wrote the manuscript. All authors revised and commented on the manuscript. **Competing interests:** The authors declare that there are no competing financial interests. **Data and materials availability:** Data from the main text and supplementary materials are available through the NIST public data repository (29).

SUPPLEMENTARY MATERIALS

science.sciencemag.org/content/364/6443/875/suppl/DC1
Supplementary Text
Figs. S1 to S9
Tables S1 to S3
References (30–40)

7 February 2019; accepted 8 May 2019
10.1126/science.aaw9415